Carbon fiber composites inspection and defect characterization using active infrared thermography: numerical simulation and experimental results

HENRIQUE FERNANDES[1,3,*], HAI ZHANG[2], ALISSON FIGUEIREDO[3], CLEMENTE IBARRA-CASTANEDO[2], GILMAR GUIMARARES[3], AND XAVIER MALDAGUE[2]

[1] Department of Computer Science, Federal University of Uberlandia, 2121 Avenida Joa Naves de Avila, Uberlandia, 38400-902, Brazil
[2] Department of Electrical and Computer Engineering, Computer Vision and Systems Laboratory, Laval University, 1065 av. de la Médecine, Québec, G1V 0A6, Canada
[3] Department of Mechanical Engineering, Federal University of Uberlandia, 2121 Avenida Joa Naves de Avila, Uberlandia, 38400-902, Brazil
* Corresponding author: henrique.fernandes@ufu.br

Composite materials are widely used in the industry. One of the reasons is because they have strength and stiffness comparable to metals with the added advantage of significant weight reduction. Infrared thermography (IT) is a safe non-destructive testing (NDT) technique that has a fast inspection rate. In active IT an external heat source is used to stimulate the material being inspected in order to generate a thermal contrast between the feature of interest and the background. In this paper carbon fiber-reinforced polymers (CFRP) are inspected using IT. More specifically, carbon/PEEK (Polyether ether ketone) laminates with square Kapton® inserts of different sizes and at different depths are tested with three different IT techniques: pulsed thermography, vibrothermography and line scan thermography. The finite element method (FEM) is used to simulate the pulsed thermography experiment. Numerical results displayed a very good agreement with experimental results. © 2016 Optical Society of America

OCIS codes: *(120.4290) Nondestructive testing; (110.3080) Infrared imaging; (100.2000) Digital image processing.*

http://dx.doi.org/10.1364/ao.XX.XXXXXX

1. INTRODUCTION

The use of composite materials, or composites, in the aeronautic industry has grown in recent years. Manufacturers have expanded the use of composites to the fuselage and wings because composites are typically lighter and more resistant to corrosion than are the metallic materials that have traditionally been used in airplanes. An example of the use of composites in commercial aircrafts is the *C Series* aircraft from Bombardier. It contains 70% advanced materials comprising 46% composite materials and 24% aluminium-lithium which allows for a 15% lower seat-mile cost and a significant reduction in maintenance costs [1]. This increasing demand motivates the industry to not only develop better and more cost efficient techniques to manufacture these materials but also to develop techniques to inspect and assure the quality of these materials during their lifetime.

In this paper, infrared thermography (IT) is used to detect delaminations (artificial inserts) placed on different layers of a carbon fiber-reinforced polymer (CFRP) flat laminate prior to moulding. Three different active IT techniques were

applied: pulsed thermography (PT), line scan thermography (LST) and vibrothermography (VT). Data was processed with principal component thermography (PCT) and pulsed phase thermography (PPT). Results, both qualitative and quantitative, showed that it is possible to detect defect insertions of different sizes at different depths using all techniques as well as that it is possible to estimate insertions' depth using the phase profiles obtained with PPT.

Additionally, a numerical model was created using COMSOL Multiphysics® in order to simulate the PT inspection and validate the experimental results. Results obtained with the numerical model were later processed with PCT and then compared with the results obtained with the PT experiment.

The remainder of this paper is organized as follows: the next section presents three active thermography approaches (PT, LST and VT); in section 3, two infrared image processing techniques are detailed (PCT and PPT); in section 4, the experimental setups are shown as well as the inspected sample detailed; section 5 shows the computational model created to simulate the inspections; the obtained results are presented in

section 6 and final remarks are made in section 7.

2. ACTIVE THERMOGRAPHY

In active thermography an external heat source is required to stimulate the material being inspected generating a thermal contrast between the feature of interest and the background. The active approach is adopted in many cases given that the inspected parts are usually in equilibrium with the surroundings [2].

Three different active IT techniques are used. The first two approaches use optical sources with different scanning modes. The first active approach tested is a static surface scanning inspection in reflection mode: the classical pulsed thermography configuration (PT). The second one is a dynamic line scanning technique where the energy source and camera are in movement with regards to the test sample (LST). The last active IT approach tested uses a mechanical source (ultrasound excitation) to generate heat in the sample being inspected. This last approach is commonly called vibrothermography (VT). Results obtained are quantified and compared. Next, we briefly describe the infrared thermography techniques applied in this paper and later present some results.

A. Pulsed thermography - PT

In pulsed thermography (PT) [3–8], the specimen surface is submitted to a heat pulse using a high power source such as photographic flashes. A heat pulse can be though as the combination several periodic waves at different frequencies and amplitudes. After the thermal front come into contact with the specimen's surface, a thermal front travels from the surface through the specimen. As time elapses, the surface temperature will decrease uniformly for a piece without internal flaws (e.g. sound area). On the contrary, subsurface discontinuities (e.g. porosity, delaminations, disbonds, fiber breakage, inclusions, etc.) can be considered as barriers to heat flow, which produce abnormal temperature patterns on the surface of the sample. This abnormal temperature distribution can be detected with an infrared (IR) camera.

The 1D solution of the Fourier equation for the propagation of a Dirac heat pulse, i.e. an ideal waveform defined as an intense unit-area pulse of so brief duration that no measuring equipment is capable of distinguishing it from even shorter pulses [9], in a semi-infinite isotropic solid by conduction has the form [10]:

$$T(z,t) = T_0 + \frac{Q}{\sqrt{k\rho C_p \pi t}} \exp\left(-\frac{z^2}{4\alpha t}\right) \tag{1}$$

where Q is the energy absorbed by the surface (J/ m^2), T_0 is the initial temperature (K), α is the thermal diffusivity (m^2 / s), t is the time (s), k is the thermal conductivity (W m^{-1} K), C_p is the specific heat (J kg^{-1} K), ρ is the density (kg/m^3) and z is the depth (m).

A Dirac heat pulse is composed of periodic waves at all frequencies and amplitudes. Although it is not possible to reproduce such a waveform in practice, a heat pulse provided by a powerful source such a photographic flash having approximately a square shape, can be used. In this case, the signal is composed by periodic waves at several (but not all) frequencies. The shorter the pulse the broader the range of frequencies.

PT is fast and straightforward as illustrated in Figure 1. Flashes can be used to heat up the specimen's surface, after
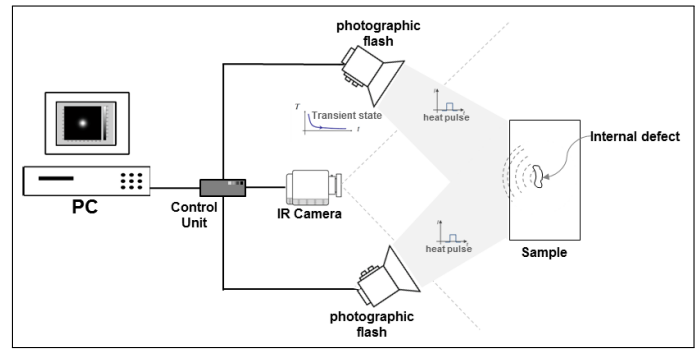

Fig. 1. PT schematic set-up.

what, the thermal changes are recorded with an IR camera. A synchronization unit is needed to control the time between the launch of the thermal pulse and the recording with the IR camera. Data is stored as a 2D matrix where x and y are the spatial coordinates, and t is the time. Temperature decreases approximately as $t^{1/2}$ (at least at early times), except for the defective areas, where the cooling rate is different. Two modes are showed in Figure 2: reflection and transition. The temperature decreasing profile is different depending on what mode is used. Figure 2(a) shows an schematic representation of a PT inspection in reflection mode and Figure 2(b) shows the respective profiles of temperature decay of a defective and a sound area. Figure 2(c) shows an schematic representation of a PT inspection in transmission mode and Figure 2(d) shows the respective profiles of temperature decay of a defective and a sound area.

PT is probably the most extensively investigated approach because of it is fast (from a few seconds for high conductivity
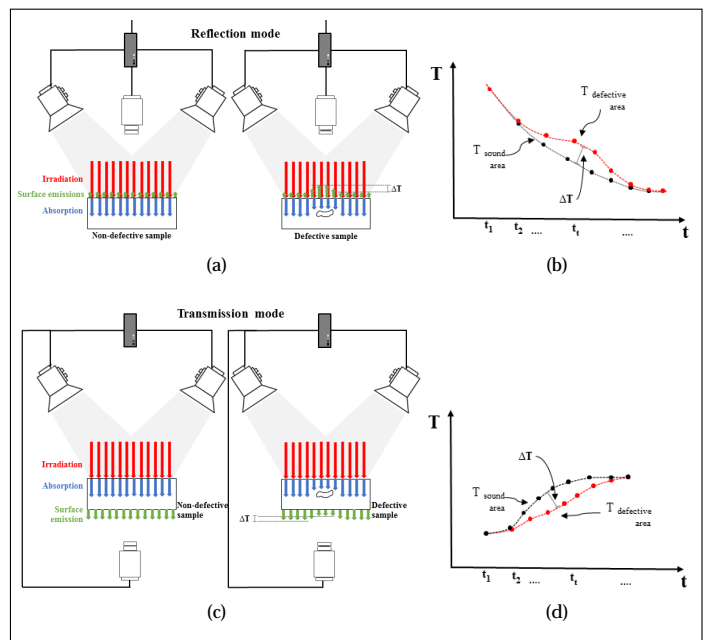

Fig. 2. PT set-up and temperature profiles for a defective and non-defective areas. (a) PT in reflection mode, (b) temperature profiles of an inspection in reflection mode, (c) PT in transmission mode, and (d) temperature profiles of an inspection in transmission mode.
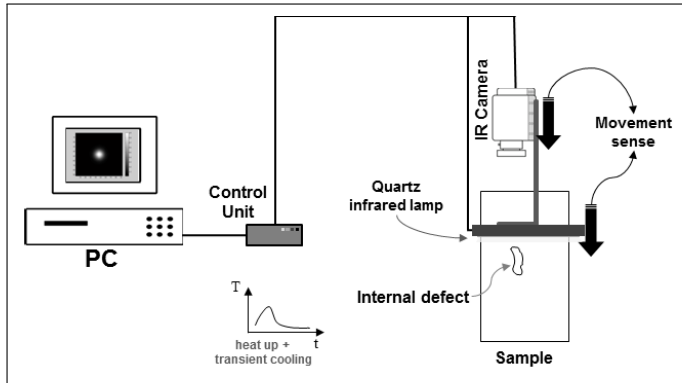
Fig. 3. LST schematic set-up.

materials to several seconds for low conductivity materials) and easy to deploy. Raw PT data however, is difficult to handle and analyze. There are a great variety of processing techniques that have being developed to enhance the subtle IR signatures. The techniques used in this paper to enhance the IR signatures are described in Section 3.

B. Line scan thermography - LST

Line scan thermography (LST) [11–14] is a dynamic active thermography technique, which can be employed for the inspection of materials by heating a component, line-by-line, while acquiring a series of thermograms with an infrared camera. This can be done in two ways, either the thermographic head, consisting of an infrared camera and an energy source, moves along the surface while the part is motionless [14], or it may be the component that is in motion while the thermographic head stands still [12]. In both cases, the thermal history for every pixel or line of pixels can be precisely tracked by controlling the heating source speed and the rate of data acquisition. In the original acquisition sequence, the inspected sample appears to be moving so the sequence must be reconstructed in order to have the variation on time and not on space.   The reconstructed matrix is obtained by following the temporal evolution of every pixel line independently, in such a way that, a given pixel line of the original sequence is recovered frame by frame (through time) and reallocated into a new sequence of images. Figure 3 shows a possible set-up for a LST inspection. In Figure 3 the thermographic head is composed of an infrared camera and a heat source. The thermographic head moves in one sense (top to bottom) covering the entire surface of the sample to be inspected while the latter remains motionless.

C. Vibrothermography - LST

Vibrothermography (VT), also known as ultrasound thermography, utilizes mechanical waves to directly stimulate internal defects, contrary to optical methods (e.g.   PT an LST), which heat the surface of the material [15–18]. Figure 4 shows a schematic set-up of a VT inspection. The mechanical waves injected into the specimen travel through the material and dissipate their energy mostly at the defects' interface, thus heat is locally released [19]. Heating is generated via three mechanisms: frictional rubbing, plastic deformations and viscoelastic losses. The thermal waves then travel by conduction to the surface where they can be detected with an IR camera.

VT is extremely fast, although it is necessary to relocate the transducer (and to immobilize the specimen again) to cover a large area for inspection. Hence, VT is more suitable for relatively small objects. It is the most appropriate technique to inspect some types of defects, e.g. micro cracks [20]. On the contrary, it does not perform very well in some other cases in which application of optical techniques are straightforward, e.g. water detection. Nonetheless, probably the most inconvenient aspect of VT is the need of holding the specimen. On the other hand, there is only minimal heating of the inspected specimen since energy is usually dissipated mostly at the defective areas, although there is some localized heating at the coupling and clamping points.

3. INFRARED IMAGE PROCESSING

A. Principal Component Thermography - PCT

In principal component thermography (PCT) [21], the data sequence is decomposed into a set of orthogonal statistical modes (known as Empirical Orthogonal Functions or EOFs) obtained through Singular Value Decomposition (SVD). The most meaningful information is placed in the firsts EOF images.

The SVD of a MxN matrix A, where $M > N$, can be calculated as follows:

$$A = URV^T \qquad (2)$$

where U is a MxN orthogonal matrix, R being a diagonal NxN matrix (with singular values of A present in the diagonal), V^T is the transpose of a NxN orthogonal matrix (characteristic time) as proposed in [21].

Hence, in order to apply the SVD to thermographic data, the 3D thermogram matrix representing time and spatial variations has to be reorganised as a 2D MxN matrix A. This can be done by rearranging the thermograms for every time as columns in A, in such a way that time variations will occur column-wise while spatial variations will occur row-wise. Under this configuration, the columns of U represent a set of orthogonal statistical modes known as empirical orthogonal functions (EOF) that describe the data spatial variations. On the other hand, the principal components (PCs), which represent time variations, are arranged row-wise in matrix V^T. The first EOF will represent the most characteristic variability of the data; the second EOF will contain the second most important variability, and so on. Usually, original data can be adequately represented with only a few EOFs. Typically, an infrared sequence of 1000 images can be replaced by 10 or less EOFs.

B. Pulsed Phased Thermography - PPT

In pulsed phase thermography (PPT), originally proposed by [22] and recently reviewed by [23], data is transformed from
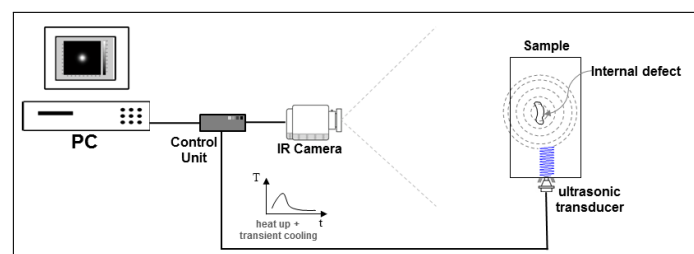

Fig. 4. VT schematic set-up.

the time domain to the frequency spectra using the 1D discrete Fourier transform (DFT):

$$F_n = \Delta t \sum_{k=0}^{N-1} T(k\Delta t) exp^{(-j2\pi nk/N)} = Re_n + Im_n \quad (3)$$

where T is the temperature, j is the imaginary number, n designates the frequency increment ($n = 0, 1, ...N$), Δt is the sampling increment, and Re and Im are the real and imaginary parts of the transform respectively. In this case, real and imaginary parts of the complex transform are used to estimate the amplitude and the phase as described in [24]:

$$A_n = \sqrt{Re_n^2 + Im_n^2} \quad (4)$$

$$\phi_n = tan^{-1}\left(\frac{Im_n}{Re_n}\right) \quad (5)$$

DFT can be applied to any waveform. The phase, equation 5, is of particular interest in NDT given that it is less affected than raw thermal data by environmental reflections, emissivity variations, non-uniform heating, and surface geometry and orientation. These phase characteristics are very attractive not only for qualitative inspections but also for quantitative characterization of materials.

A linear relationship exists between defect depth z and the inverse square root of the blind frequency (which can be observed form experimental data). According to [25], blind frequency (f_b) is the frequency at which the phase contrast is enough for a defect to be visible, i.e., at frequencies higher than f_b, it is not possible to detect it. The thermal diffusion length (μ), described by [26], can be used to fit experimental data and estimate the depth (z) as proposed by [27]:

$$z = C_1 \sqrt{\frac{\alpha}{\pi.f_b}} = C_1\mu \quad (6)$$

where the thermal diffusion length is $\mu = 2\alpha/\omega$ (m), ω (rad/ s) is the angular frequency, α is the thermal diffusivity of the material, f_b (Hz) is the blind frequency and C_1 is an empirical constant where has been observed that $1.5 < C_1 < 2$ when working with the phase, with $C_1 = 1.82$ typically adopted in several work such as in [28, 29].
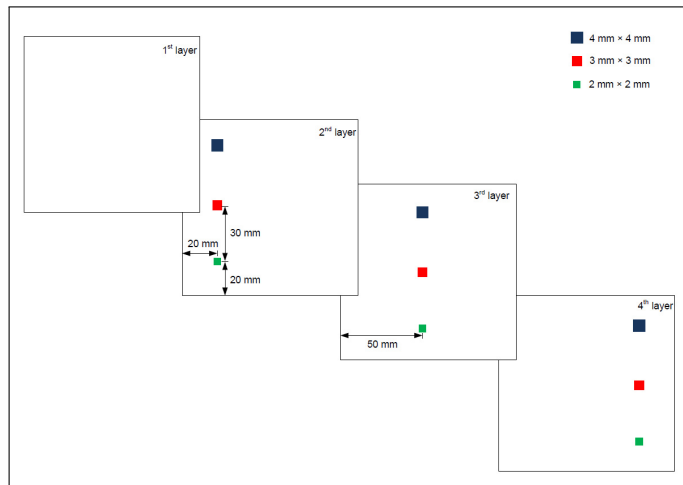

Fig. 5. Position of the artificial inserts on the layers of the laminate.
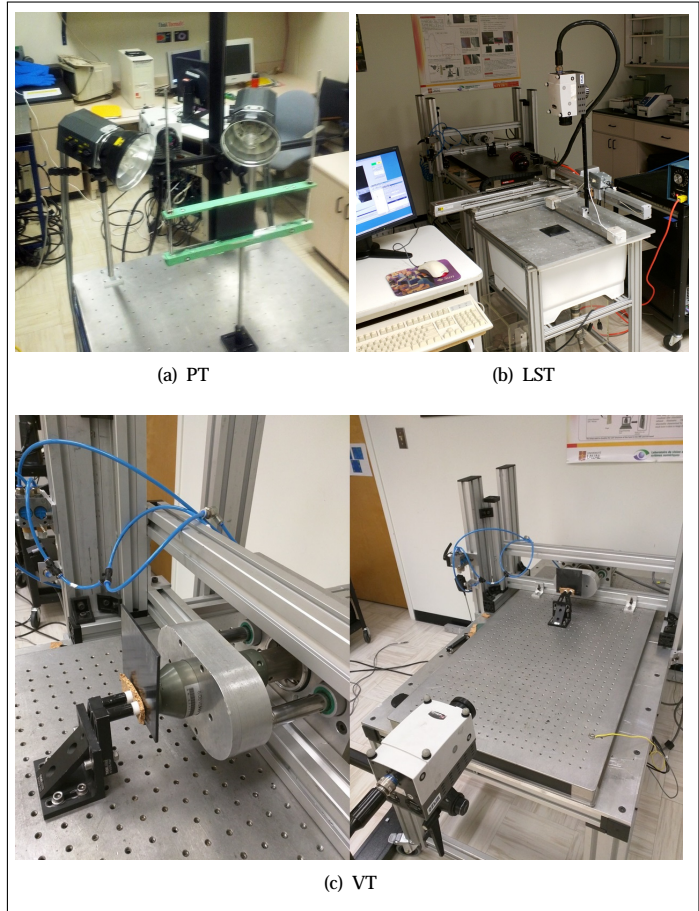

(a) PT

(b) LST

(c) VT

Fig. 6. Laboratory setups.

4. EXPERIMENTAL SET-UP AND INSPECTED SAMPLE

In this paper, infrared thermography (IT) is used to detect delaminations (artificial inserts) placed on different layers of a carbon fiber-reinforced polymer (CFRP) flat laminate prior to moulding. The part inspected is a 100x100 mm unidirectional laminate manufactured with carbon/PEEK (*Polyether-Ketone-Ketone*). It has a fiber volume fraction of 61%. Levy presents in Appendix F of his thesis [30] a complete list of the parameters of the material. The thermal properties of the material are listed in Table 1.

The laminate layup is $[0_2/90_2]_6$, i.e. it has 24 layers where the first two layers have 0° oriented fibers and the third and fourth layers have 90° oriented fibers. A prepreg prior to mould is 0.16 mm thick while, after moulding, it is about 0.13 mm thick. Artificial inserts made of *Kapton*® tape (0.06 mm thick) were placed in different regions of the laminate prior to molding. They have three different sizes: 4x4 mm, 3x3 mm and 2x2 mm. Their positions prior to moulding can be seen in Figure 5.

Figure 6 shows the experimental setups used to inspect the part in the laboratory. For all inspections a mid-wave infrared (MWIR) camera (FLIR Phoenix, InSb, 3-5 μm, 640x512 pixels windowed to 320x256 pixels in some cases) at a frame rate of 55 Hz (for PT and VT experiments) and 220 Hz (for LST experiments) was used to record the temperature profiles. In the pulsed thermography inspection case, two photographic flashes (with pulse duration of 5 ms and producing 6.4 kJ per flash) were used to heat the sample. Images were recorded in

**Table 1.** Thermal properties of carbon/PEEK [31].

|	Property		Value	
k:	Thermal conductivity	Longitudinal	5.65	[W/mK]
		Transverse	0.35	[W/mK]
C_p:	Specific heat[a]		1310	[J/kgK]
ρ:	Density		1584	[kg/m^3]

[a] *at constant pressure.*

reflection mode. In the second case, the line scan inspection, a thermographic head was used consisting of the same MWIR camera used for the PT inspection and an electrical actuator with a quartz infrared lamp (1600 W). Samples were kept motionless while the thermographic head moved at a constant speed of 50 and 100 mm/ s. In the vibrothermography case, the transducer horn was pressed against the sample and a burst of ultrasound waves (15 - 25 kHz, 2200 W) at a modulation frequency of 0.5 Hz and with amplitude modulated between 10-60% of maximum power was delivered to the sample for each inspection. The plate was inspected twice due to the position of the inclusions on the sample and the transducer horn contact spot. In the VT experiments, the sample was rotated 180° clockwise thus, in the first VT experiment the row of largest inserts appears on the image and in the second VT experiment the row of smallest inserts appears while the middle row is repeated in both experiments. However, the second VT image result is presented rotated in this paper. Thus, the row with the smallest inserts appears on the bottom of the image result.

5. COMPUTATIONAL MODEL

The finite element method is a powerful numerical tool that enables the solution of complex nonlinear, nonsymmetrical mathematical problems governed by partial differential
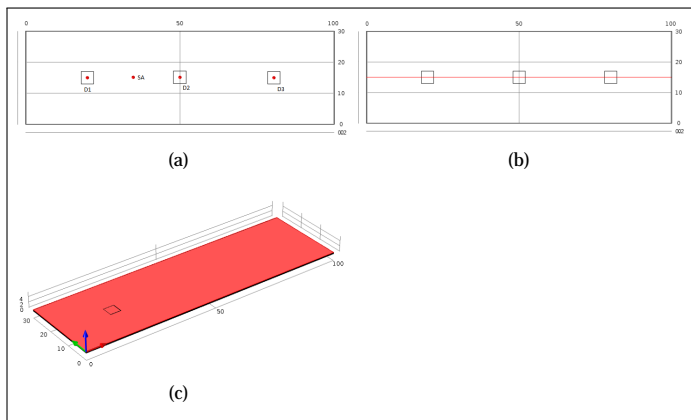

Fig. 7. Geometry created with COMSOL®. (a) Point D1 indicates the XY position of the defect 1 which is at z = 0.13 mm, point D2 indicates the XY position of the defect 2 which is at z = 0.26 mm, point D3 indicates the XY position of the defect 3 which is at z = 0.39 mm and point SA indicates the XY position of a sound area. (b) Position of a line crossing all three delaminations at z = 0 and y = 15 mm. (c) Surface at z = 0.
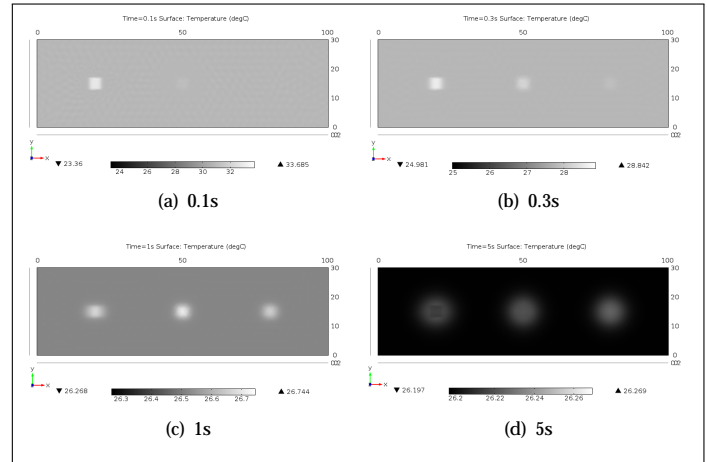

Fig. 8. Temperature distribution on the surface XY in different times.

equations such as the one of heat transfer by conduction, convection and radiation with temperature dependent thermal properties of materials involved. In order to solve the given differential equation, a 3D model of the sample's surface geometry corresponding to the first row of defects of the tested sample was defined and its calculation domain divided into finite elements that represent base elements on which the equation solutions are found. The numerical modeling was performed using the software COMSOL Multiphysics® 4.3 from Comsol, Inc. The thermal properties of the material are listed in Table 1.

The PT experiment was modelled in order to confirm the results obtained experimentally. In this sense, a short pulse of 0.01 s was used to heat up the surface of the model with 1800 W (transient heating) with COMSOL®. The solution for the heating equation was computed for 10 s with an interval of 0.018 s between each solution. This interval was selected in order to follow the camera frame rate used in the PT experiments, i.e. 55 Hz. A fine mesh was used. As mentioned
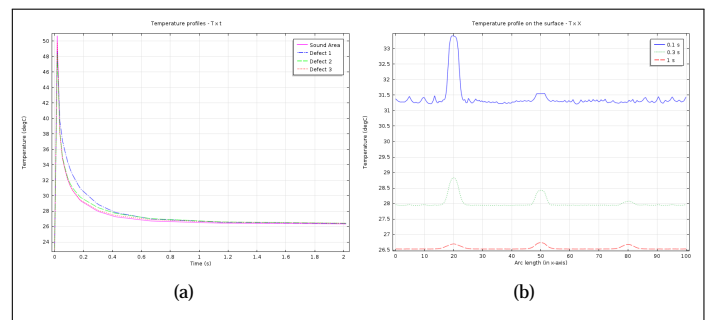
Fig. 9. Temperature profiles obtained with the numerical model for a PT inspection. (a) Temperature x time: on the surface of the sample. First region corresponds to a sound area region, second region corresponds to the first defect (which is at 0.13 mm to the surface), third region corresponds to the second defect (which is at 0.26 mm to the surface), and the last region corresponds to the third defect (which is at 0.39 mm to the surface); (b) Temperature x x-axis: temperature distribution along x-axis at y = 15 mm at different times (0.1, 0.3 and 1 s).
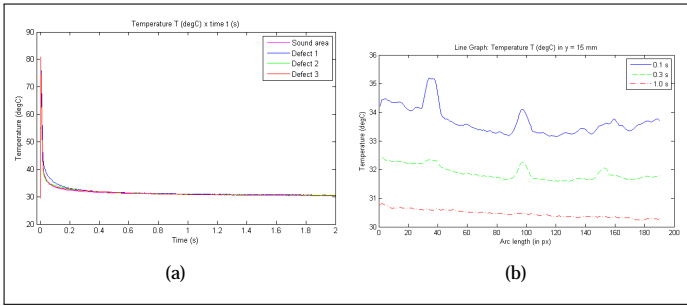
Fig. 10. Temperature profiles obtained experimentally for a PT inspection. (a) Temperature x time: on the surface of the sample. First region corresponds to a sound area region, second region corresponds to the first defect (which is at 0.13 mm to the surface), third region corresponds to the second defect (which is at 0.26 mm to the surface), and the last region corresponds to the third defect (which is at 0.39 mm to the surface); (b) Temperature x x-axis: temperature distribution along x-axis at y = 15 mm at different times (0.1, 0.3 and 1 s).

before, the solution was computed only for a third of the area of the geometry, i.e. the first row of defects (4x4 mm). Figure 7 shows the position of the defects, a sound area, the row of defects and the surface (z = 0) of the geometry created with COMSOL®.

6. RESULTS AND DISCUSSION

A. Qualitative

Figure 8 shows the temperature distribution obtained with COMSOL® on the surface of the model, i.e., z = 0, of several seconds. The thermal signature of the defects are clearly apparent on the surface. Figure 7(c) indicates the region corresponding to the plotted surface. Figure 9(a) shows the temperature profiles of the defects' regions over time obtained also with numerical model (only the first two seconds are shown). Figure 7(a) indicates the positions of the plotted points. Figure 9(b) shows the temperature profiles on the surface in the region corresponding to the line crossing all three defects at different times.

Figure 10 shows, for the PT case, the temperature profiles obtained experimentally of the defects' regions over time (only the first two seconds are shown). Also, it shows the temperature profile on the surface in the region corresponding to the line crossing all three defects. The results obtained experimentally are very close to those obtained during the simulations (see Figure 9(a) and Figure 9(b) also for the PT case).

The sequences acquired in each experiment were processed using principal component thermography (PCT) [21]. In this technique the data sequence is decomposed into a set of orthogonal statistical modes (known as Empirical Orthogonal Functions or EOFs) obtained through Singular Value Decomposition (SVD). The most meaningful information is placed in the firsts EOF images. Figure 12 shows the second EOF images of the inspections using the three different techniques (PT, LST and VT).

For the LST inspection, a previous step was performed to rearrange the data into a new pseudo-static sequence where changes occur in time and not in space (the plate appears to be motionless like in a PT inspection). A procedure to obtain this

pseudo-static sequence is described by Ibarra-Castanedo [32]. As it can be seen in Figure 12, the three techniques successfully detect all delaminations.

PCT was also applied in the results obtained with the numerical model (model of the PT experiment). The time temperature profiles on the surface (z = 0) were exported from COMSOL® and then the EOF images were calculated. Figure 11 shows the second EOF image of the solution provided by COMSOL®. If one compares Figure 12(a) and Figure 11 it can be observed that results obtained with the numerical model confirm the results obtained with the PT experiment.

B. Quantitative

For the PT inspections, quantitative results were also calculated. For the 3x3 mm delamintations, i.e. inserts in the second row, the estimated depth of each insert was calculated based on the phase images obtained with PPT. Equation 6 was used for this purpose.

PPT was applied on the raw sequence and blind frequencies (fb) of each defect were calculated. The respective blind frequencies, calculated based on the phase profiles, for the defects #1 (insert on the 2nd layer at depth 0.13 mm), #2 (insert on the 3rd layer at depth 0.26mm), and #3 (insert on the 4th layer at depth 0.39mm), are respectively $fb_1 = 19$Hz, $fb_2 = 7$ Hz, and $fb_3 = 2.6$ Hz, which give, by applying Equation 6 with $\alpha_{CFRP} = 4.2x10^{(-7)}$ m^2 / s and $C_1 = 1.82$, estimated depths of 0.151 mm, 0.2488 mm and 0.4082 mm, respectively. Based on the specifications provided in Figure 5, the estimated depths are close to the reported nominal depths. Figure 13 shows the phase profiles of each one of the three 3x3 mm inserts with a respective sound area defined just next to the insert. The crossing of the insert phase profile with the sound area phase profile indicates the blind frequency of the insert which was used to estimate its depth.

7. CONCLUSIONS

In this paper, three active IT techniques were used to inspect a CFRP laminate with artificial inserts. Inserts of different sizes and on different layers (depths) were detected by all techniques. Results were quantified and compared for the PT inspection. The depths of inserts located at 0.13, 0.26 and 0.39 mm from the surface were successfully estimated using phase profiles obtained with PPT with a maximum error of 16.15%.

On the qualitative side, PT and VT showed an increased defect contrast with respect to LST. Nevertheless, the presented LST results suggest that, for cases where the use of PT is restricted, e.g., when one is inspecting complex shaped parts, the use of LST is a viable solution. In this case, the thermographic head would move in a controlled fashion (being able to move in all dimensions), for instance using a robot [32], in order to follow the shape of the sample.
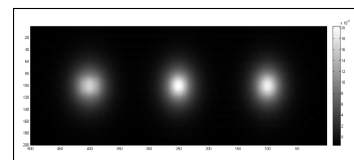
Fig. 11. Results obtained with PCT from the numerical model of the simulated PT experiment.
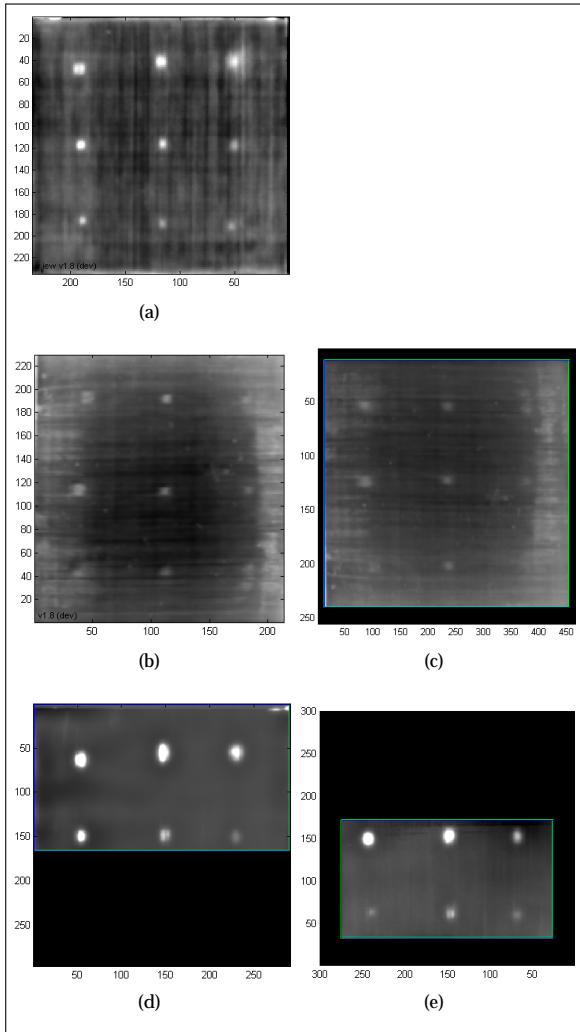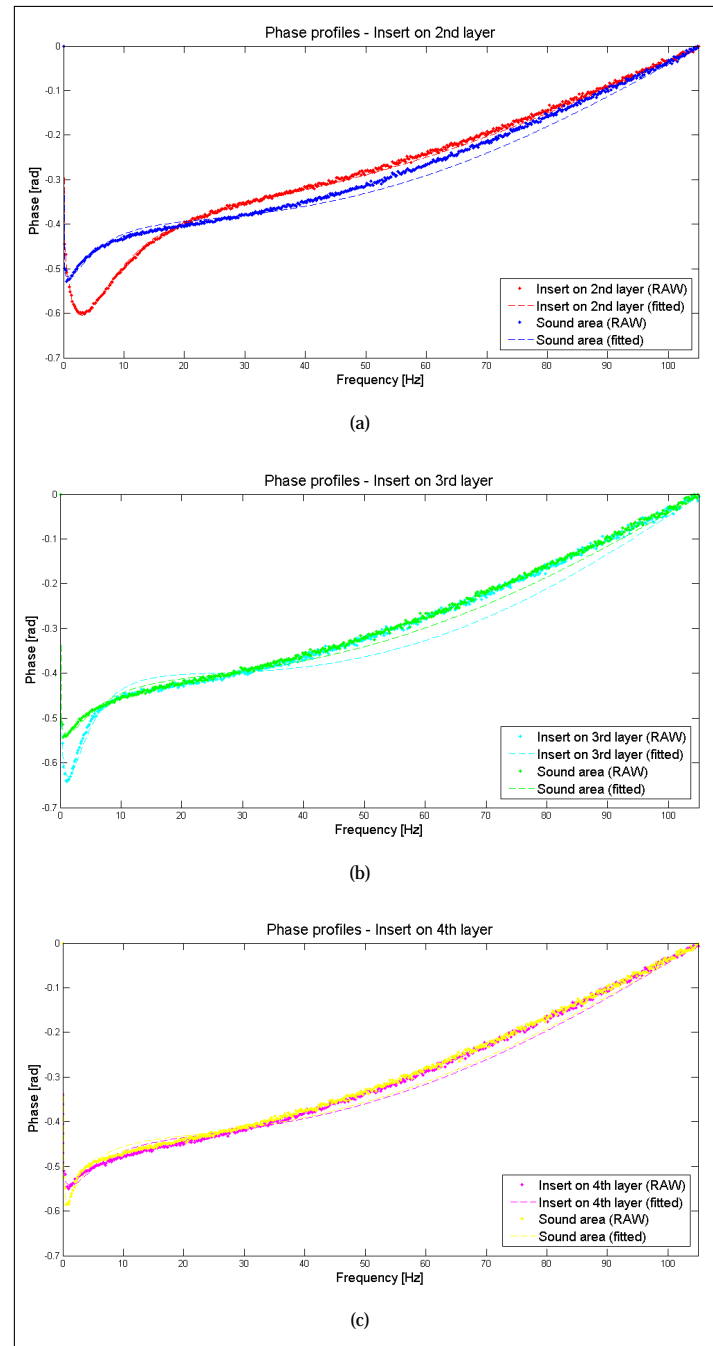
Fig. 12. Results obtained with PCT for experiments (x-axis and y-axis are in pixels) – (a) PT, (b) LST thermographic head moving at 100 mm∕s, (c) LST thermographic head moving at 50 mm∕s, (d) VT showing the biggest inserts and (e) VT showing the smallest inserts.

Additionally, PCT was applied in the results obtained with the numerical model for the PT case. The time temperature profiles on the surface of the geometry were used to calculate the EOF images. The PCT result obtained for the PT experiment (Figure 12(a)) was then compared with PCT result obtained for the numerical solution (Figure 11). As it could be observed, PCT provided very similar results for both experimental and numerical cases.

Fig. 13. Phase profiles (defect and sound area) obtained with PPT for PT experiments. (a) Phase profiles for the 3x3 mm delamination on the 2nd layer – approximately at 0.13 mm ($fb_1 = 19$ Hz), (b) phase profiles obtained with PPT for the 3x3 mm delamination on the 3rd layer – approximately at 0.26 mm ($fb_2 = 7$ Hz), and (c) phase profiles for the 3x3 mm delamination on the 4th layer – approximately at 0.39 mm ($fb_3 = 2.6$ Hz).

REFERENCES

1. Bombardier, "C series http://www.cseries.com," (June 2015).
2. X. P. V. Maldague, *Theory and practice of infrared technology for nondestructive testing* (Wiley-Interscience, New York, 2001), 1st ed.
3. S. M. Shepard, "Advances in pulsed thermography," in "Proc. SPIE, Thermosense: Thermal Infrared Applications XXVIII," , vol. 4360 (2001), vol. 4360, pp. 511–515.
4. D. L. Balageas, "Defense and illustration of time-resolved pulsed thermography for nde," Quantitative InfraRed Thermography Journal **9**, 3–32 (2012).
5. F. Lopez, C. Ibarra-Castanedo, V. P. Nicolau, and X. Maldague, "Optimization of pulsed thermography inspection by partial least-squares regression," NDT & E International, **66**, 128 – 138 (2014).
6. H. Fernandes, H. Zhang, and X. Maldague, "An active infrared thermography method for fiber orientation assessment of fiber-reinforced composite materials," Infrared Physics & Technology **72**, 286 – 292 (2015).
7. V. P. Vavilov and D. D. Burleigh, "Review of pulsed thermal NDT: Physical principles, theory and data processing," NDT & E International, **73**, 28 – 52 (2015).
8. H. Zhang, L. Yu, U. Hassler, H. Fernandes, M. Genest, F. Robitaille, S. Joncas, W. Holub, Y. Sheng, and X. Maldague, "An experimental and analytical study of micro-laser line thermography on micro-sized flaws in stitched carbon fiber reinforced polymer composites," Composites Science and Technology **126**, 17 – 26 (2016).
9. R. Bracewell, *The Fourier Transform and Its Applications* (McGraw-Hill, USA, 1966).
10. H. S. Carslaw and J. C. Jaeger, *Conduction of Heat in Solids* (Clarendon Press, Oxford, 1986), 2nd ed.
11. C. Gruss and D. Balageas, "Theoretical and experimental applications of the flying spot camera," in "Proceedings of the QIRT 92," (1992), pp. 19–24.
12. B. Oswald-Tranta and S. Shepard, "Comparison of pulse phase and thermographic signal reconstruction processing methods," in "Proc. SPIE, Thermosense XXXV," , vol. 8705 (2013), vol. 8705, pp. 87050S1–9.
13. D. F. Woolard and K. E. Cramer, "The thermal photocopier: A new concept for thermal ndt," in "Proc. SPIE, Thermosense XXVI," , vol. 5405 (2004), vol. 5405, pp. 366–373.
14. D. F. Woolard and K. E. Cramer, "Line scan versus flash thermography: Comparative study on reinforced carbon-carbon," in "Proc. SPIE, Thermosense XXVII," , vol. 2782 (2005), vol. 2782, pp. 315–323.
15. S. Shepard, T. Ahmed, and J. R. Lhota, "Experimental considerations in vibrothermography," in "Proc. SPIE, Thermosense XXVID," , vol. 5405 (2004), vol. 5405, pp. 332–335.
16. A. Mian, G. Newaz, X. Han, T. Mahmood, and C. Saha, "Response of sub-surface fatigue damage under sonic load a computational study," Composites Science and Technology **64**, 1115–1122 (2004).
17. M. J. Rothenfusser and C. Homma, "Acoustic thermography: vibrational modes of cracks and the mechanism of heat generation," in "AIP Conference Proceedings," , vol. 760 (2005), vol. 760, pp. 624–631.
18. J. Renshaw, J. C. Chen, S. D. Holland, and R. B. Thompson, "The sources of heat generation in vibrothermography," NDT & E International **44**, 736–739 (2011).
19. L. Pieczonka and M. Szwedo, "Vibrothermography," in "Advanced Structural Damage Detection: From Theory to Engineering Applications," , T. Stepinski, T. Uhl, and W. Staszewski, eds. (Wiley, 2013), chap. 9, pp. 251–275.
20. H. Fernandes, C. Ibarra-Castanedo, H. Zhang, and X. Maldague, "Thermographic non-destructive evaluation of carbon fiber-reinforced polymer plates after tensile testing," Journal of Nondestructive Evaluation, **34**, 1 – 10 (2015).
21. N. Rajic, "Principal component thermography for flaw contrast enhancement and flaw depth characterisation in composite structures," Composite Structures **58**, 521–528 (2002).
22. X. Maldague and S. Marinetti, "Pulse phase thermography," Journal of Applied Physics **79**, 2694–2698 (1996).
23. C. Ibarra-Castanedo and X. Maldague, "Review of pulse phase thermography," in "Proc. SPIE - Thermosense: Thermal Infrared Applications XXXVII," , vol. 9485 (2015), vol. 9485, pp. 94850T–94850T–10.
24. C. Ibarra-Castanedo and X. Maldague, "Pulsed phase thermography reviewed," Quantitative InfraRed Thermography Journal **1**, 47–70 (2004).
25. W. Bai and B. S. Wong, "Evaluation of defects in composite plates under convective environments using lock-in thermography," Measurement Science and Technology **12**, 142–150 (2001).
26. G. Busse and A. Rosencwaig, "Subsurface imaging with photoacoustics," Applied Physics Letters **36**, 215–812 (1980).
27. C. Ibarra-Castanedo, "Quantitative subsurface defect evaluation by pulsed phase thermography depth retrieval with the phase," Ph.D. thesis, Faculté des études supérieurs de Université Laval (2005).
28. C. Meola and G. M. Carlomagno, "Recent advances in the use of infrared thermography," Measurement science and technology **15**, 27–58 (2004).
29. C. Meola, G. M. Carlomagno, and L. Giorleo, "The use of infrared thermography for materials characterization," Journal of materials processing Technology **155**, 1132–1137 (2004).
30. A. Levy, "Modélisation et simulation d'un écoulement sous vibration. application au soudage par ultrasons de composites à matrice thermoplastique," Ph.D. thesis, Ecole Central de Nantes (2010).
31. C. Ageorges, L. Ye, Y.-W. Mai, and M. Hou, "Characteristics of resistance welding of lap shear coupons. Part I: Heat transfer," Composites Part A: Applied Science and Manufacturing **29**, 899–909 (1998).
32. C. Ibarra-Castanedo, P. Servais, A. Ziadi, M. Klein, and X. Maldague, "Rita - robotized inspection by thermography and advanced processing for the inspection of aeronautical components," in "The 12th International Conference on Quantitative InfraRed Thermography, 7-11 July, Bordeaux, France," , D. Balageas, ed. (2014).